Article

aeroacoustics

International Journal of Aeroacoustics
0(0) 1–24

DOI: 10.1177/1475472X16659384
jae.sagepub.com

Time-resolved PIV measurements of a tip leakage flow

Marc C Jacob, Emmanuel Jondeau and Bo Li

Abstract

Time-resolved PIV and time-resolved stereo PIV measurements are carried out in the tip leakage vortex of a single non-rotating airfoil placed in the potential core of a flanged rectangular jet in free field conditions. The experiment is based on the improvement of an existing rig: a cambered airfoil (NACA5510) now mounted with a $16.5^\circ \pm 0.5^\circ$ angle of attack between two horizontal plates, a $10\ \mathrm{mm}$ gap being maintained between the airfoil tip and the lower (casing) plate. The mean flow velocity is $70\ \mathrm{m/s}$, which corresponds to a 0.2 Mach number and a chord-based Reynolds number of $933,000$. Unlike in the former experiment carried out with this rig, the boundary layer thickness is now smaller than the gap, which significantly reduces the interaction between the upstream turbulence and the airfoil leading edge as well as the resulting interaction noise. The measurements described here include the far field. The upstream flow is characterised with hotwire anemometry. LDV profiles are also obtained in the tip leakage region and compared to the PIV measurements. The experiment is also designed to provide validation data for unsteady CFD computations of the same configuration as shown in a companion paper.

Keywords

tip leakage vortex, time resolved stereo PIV, vortex identification, broadband noise

Date received: 12 March 2015; revised: 10 February 2016; accepted: 23 May 2016

Introduction

Tip clearance flows are a major concern in many industrial applications, from automotive fans to airplane turbomachines. They are not only the cause of aerodynamic losses but are also suspected to be efficient sound sources. For all these reasons, rotor tip clearance flows have been a subject of interest in turbomachinery and aeroacoustic research for a long time

Centre Acoustique LMFA, UMR CNRS 5509 – Ecole Centrale de Lyon, Université de Lyon, France

Corresponding author:
MC Jacob, Département Aérodynamique, Energétique et Propulsion (DAEP), ISAE-SupAéro, 10 av. Edouard Belin, BP 54032, F- 31055 Toulouse Cedex 4, France.
Email: marc.jacob@ec-lyon.fr

as discussed in Jacob et al.[1] In recent years, beside the research reported in Jacob et al.[1] that addresses the tip leakage flow of an isolated non-rotating airfoil, most studies are concerned with tip leakage noise in fans: several authors studied low speed fans,[2] fans near surge conditions,[3] rotating instabilities,[4] or fans with tip/casing treatments.[4] In fact, few papers are concerned with tip flows of isolated non-rotating blades, and since the experiments of Jacob et al.[1] and related computations, there have been no further studies in such academic configurations.

The new experiment discussed in the present paper is meant to complement and improve the information from the previous campaign.

- The background noise of the rig has been reduced in order to provide a better signal-to-noise ratio for the acoustic measurements.
- Moreover, PIV measurements are carried out in cross sections of the tip leakage vortex (TLV) in order to characterise its axial vorticity.
- The present paper is focused on mean flow characterisation, but the use of time-resolved (TR) PIV, provides a large amount of data that is to be more thoroughly analysed in future publications.
- The data set of this new experiment is also suitable for validation of LES or hybrid RANS/LES computations as shown in Boudet et al.[5]

In the next section, we shall describe the overall experimental set-up and indicate changes with respect to the existing rig. The inflow conditions as well as the aerodynamic installation of the airfoil are discussed in the succeeding section. The following three sections are dedicated to LDV, 2 Dimensional 2 Component (2D-2C) Time Resolved (TR) PIV and 2 Dimensional 3 Component (2D-3C) TR PIV respectively. Far field measurements are briefly discussed in the penultimate section. The last section is devoted to conclusions and ends the main body of the article.

Experimental set-up

Existing rig and rig modifications

Flow set-up. The single airfoil experiment is conducted in the large anechoic room of the ECL (10 m × 8 m × 8m) in a 0.45 m × 0.2 m rectangular open jet. The airflow is guided 2.5 m into the room by a square 0.56 m × 0.56 m and 2 m long duct with a 7.5° angle with respect to the room inlet–outlet axis. The purpose of this duct is to allow for upstream propagation and to compensate flow deviations due to the airfoil (that might damage the anechoic coating of the room). Air is supplied by a high-speed subsonic anechoic wind tunnel at Mach numbers M ranging up to 0.4.

For practical reasons however (mechanical forces onto the airfoil support, vibrations, etc.) and for numerical reasons (chord based Reynolds number: $Re_c < 10^6$), the Mach number was maintained below 0.27 (90 m/s) and the main (or reference) configuration was at M ~0.2 (70 m/s). Although these speeds may appear quite small, they are not much lower than that of an approaching aircraft for which fan broadband noise is a major sound source. Unless mentioned otherwise, the velocity will be $U_0 = 70\,\mathrm{m}/s$ and the gap $h = 10$ mm throughout the paper. The jet is flanged by two plates on the upper (hub) and lower (casing) side of the jet.

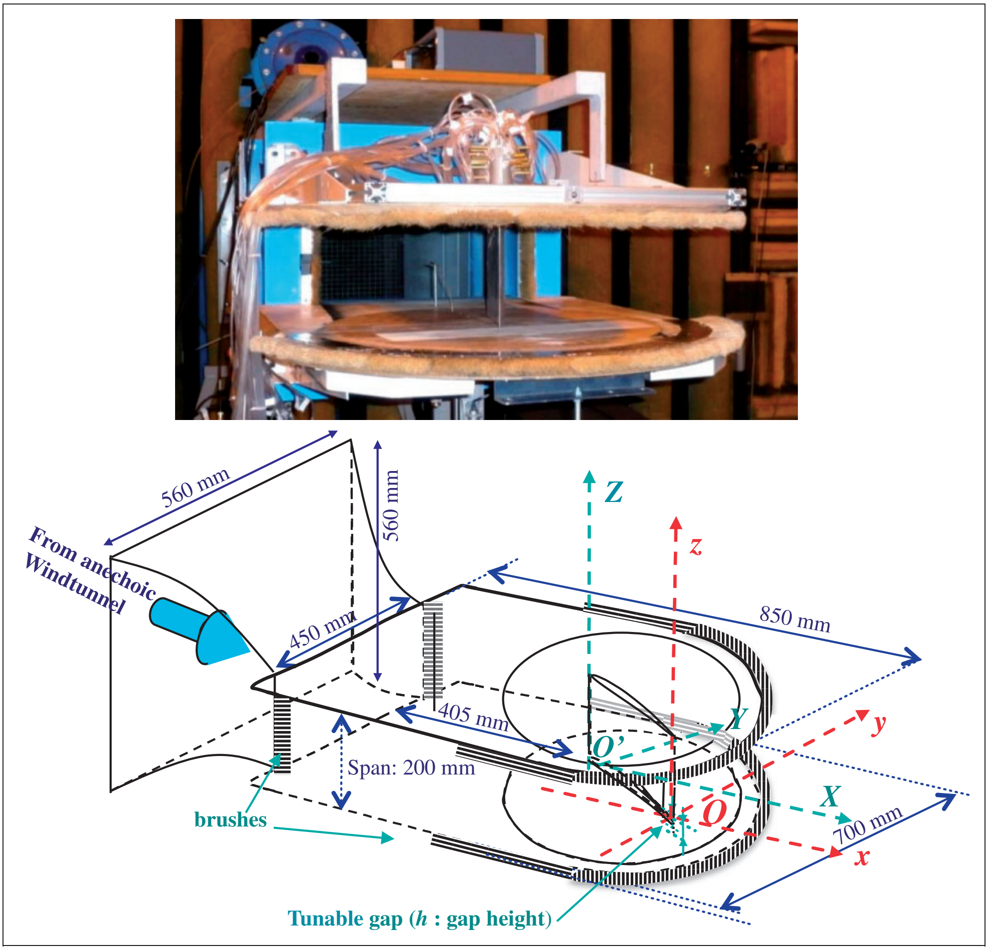

Figure 1. Picture of the experimental set-up, where the airfoil is equipped with static pressure probes and an HWA probe is in an upstream section (top). Sketch showing the two coordinate systems (bottom): the dark stripes symbolise the brushes.

Rig modifications

The experimental set-up, which is shown on Figure 1, is based on an existing rig[1,6]: an initial gap between each of the plates and the nozzle lip provided a passive suction device that allowed tuning the boundary layer thickness. The airfoil was mounted in the potential core region of the jet onto a wooden disk that was attached to the upper plate and could be turned in order to modify the angle of attack. Another disk was mounted onto the lower plate. Two disks had been designed for the lower plate: one that contained a square glass window for PIV measurements, and a wooden disk that could be equipped with probes and probe supports.

In the present experiment, the boundary layer suction device has been suppressed in order to obtain a non-tunable but much thinner boundary layer. Moreover, in order to quieten the surrounding jet flow and to reduce low frequency jet oscillations, the nozzle lips as well as the plate edges have been equipped with brushes. As a result, the turbulence level in the main flow at the jet nozzle is $u'/\ U_0\ \sim 0.5\%$. For a $U_0 = 70$ m/s nozzle outlet velocity, the boundary layer thickness is $\delta \sim 7.5$mm half a chord upstream of the airfoil instead of 18 mm. Similarly, the displacement thickness is reduced from $\delta^* \sim 1.4$ to 0.95mm.

Airfoil and reference configuration

The airfoil is a NACA5510 (chord $c = 200$ mm, span $\ell = 190$ to200 mm, thickness $e = 20$ mm, 5% camber). It is located ~ 1.5 chords downstream of the jet nozzle. There are two reference configurations: for both configurations, the geometrical angle of attack (AoA) is $16.5^\circ \pm 0.5^\circ$, the flow is uniform within 0.6%, and its speed at the nozzle outlet is $U_0 = 70$ m/s or 40 m/s. The two configurations only differ by the size of the gap, one having an $h = 10$ mm gap and the other having no gap at all, herein the "no gap configuration": although this configuration is a "self noise" configuration in the classical sense, i.e. trailing edge self noise, we will avoid to name it simply the "self noise configuration" because this term is misleading in the present case: it will indeed be shown that the tip clearance noise is also a self noise source *stricto senso* since it is located on the airfoil and is due to flow perturbations generated in the gap.

Coordinate systems

There are two coordinate systems of interest in the present study.

The first is convenient to describe the flow impinging onto the airfoil and originates on the lower plate below the airfoil leading edge (point O'). The $X-$ axis is aligned with the main flow direction, that is the nozzle axis, the Z-axis is in the spanwise (vertical) direction and is oriented from the lower to the upper plate, whereas the Y-axis is in the cross-stream direction to the left when looking into the streamwise direction.

The second coordinate system is parallel to the first, but its origin O is on the trailing edge/gap corner. For the sake of clarity, it will be labelled (O, x, y, z). The motivation for this choice originates from earlier measurements on the present rig[5]: the TLV is roughly aligned with the main incoming flow direction and the angle of its conical shape corresponds approximately to the angle of attack. Thus, the second coordinate system is almost parallel to the TLV core trajectory. This will be checked in more detail hereafter.

Inflow assessment and mean pressure

The inflow parameters were assessed using classical hot wire anemometry (HWA) as well as Laser Doppler Velocimetry (LDV).

Hot wire anemometry

The HWA device is a *Dantec* anemometer with a 55P01 *Dantec* probe mounted on a probe support. The probe calibration accounts for both velocity and temperature and is adjusted on the run with a Pitot probe and a thermal probe mounted in the vicinity of the HWA probe without perturbing the flow around the HWA probe. The signals are recorded with a 102.4 kHz and with a 45 kHz sampling frequency.

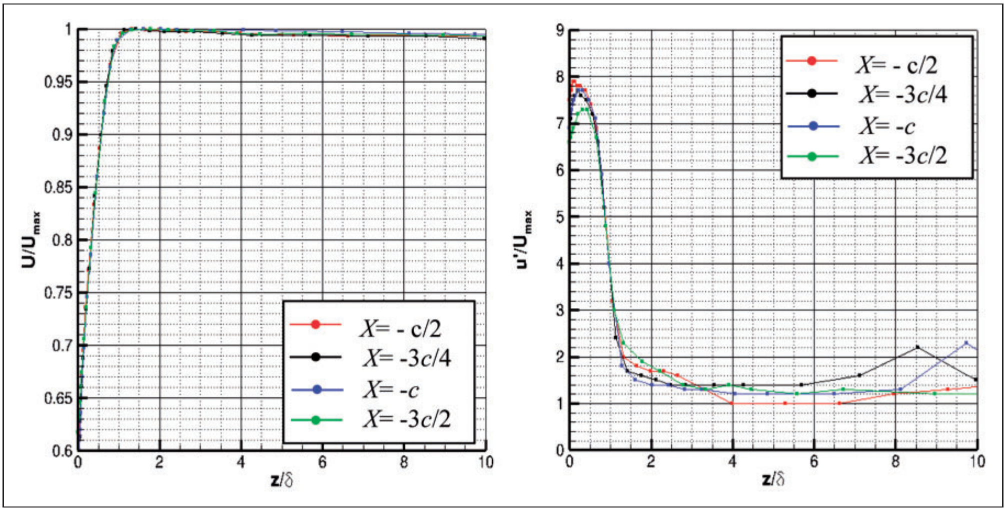

Figure 2. Stream-wise mean velocity (left) and rms velocity fluctuation (turbulence intensity) (right) upstream of the flow at $X = -c/2$; $-3c/4$, $-c$, $-3c/2$. The turbulence intensity is expressed in percentage. Profiles of the casing wall are shown in the spanwise direction, the Z coordinate is non-dimensionalised against the boundary layer thickness.

Incoming flow and mean pressure distribution at mid-span

The incoming flow is measured in four cross sections upstream of the airfoil ($X = -c/2$, $-3c/4$, $-c$, $-3c/2$).

Upstream velocity profiles and turbulence level. The left plot of Figure 2 shows the non-dimensional streamwise velocity spanwise profiles obtained with single HWA in the 10 first Boundary layer thicknesses away from the lower plate. The profiles collapse almost perfectly, and away from the plate, and the flow becomes uniform within 1%.

As shown on the right plot of this figure, away from the plate boundary layers the turbulence level drops down to about 1%, and the rise around $7-10\ \delta$ remains unclear. In the casing plate boundary layer, the turbulence level reaches about $7.4-8\%$ that is 1% less than in Boudet et al.[5] This maximum is reached between $Z/\delta \sim 0.1$ and 0.3.

Mean velocity and velocity fluctuation profiles in the cross-stream direction, which are not shown here, confirm the uniformity of the upstream velocity about one chord away from airfoil in both directions, with a turbulence dropping down to 0.5% in the central part of the flow (not shown here).

Boundary layer parameters. The main boundary layer parameters extracted from the profiles plotted on Figure 2 are summarised in Table 1.

These results are very important as they show that in the present experiment, the boundary layer in the vicinity of the airfoil is clearly thinner than the tip clearance ($h = 10$ mm). Moreover, the maximum turbulence level ($7.5-8\%$) is reached at less that $\delta/3$: thus the direct interaction noise between boundary layer turbulence and the airfoil leading edge is kept small. In particular, it is worth noting that at $X = -c/2$, the maximum is at $Z \sim 1$ mm, which is far less than the tip clearance $h = 10$ mm and at $Z = h$, the turbulence level is less

Table 1. Boundary layer thickness δ, displacement thickness δ^*, momentum thickness θ and shape factor H at four streamwise positions in the incoming flow.

	$X = -3c/2$	$X = -c$	$X = -3c/4$	$X = -c/2$
δ(/mm)	4.5	6.2	7.0	7.5
δ^*(/mm)	0.56	0.83	0.91	0.95
Θ(/mm)	0.35	0.45	0.50	0.56
H	1.62	1.82	1.84	1.70

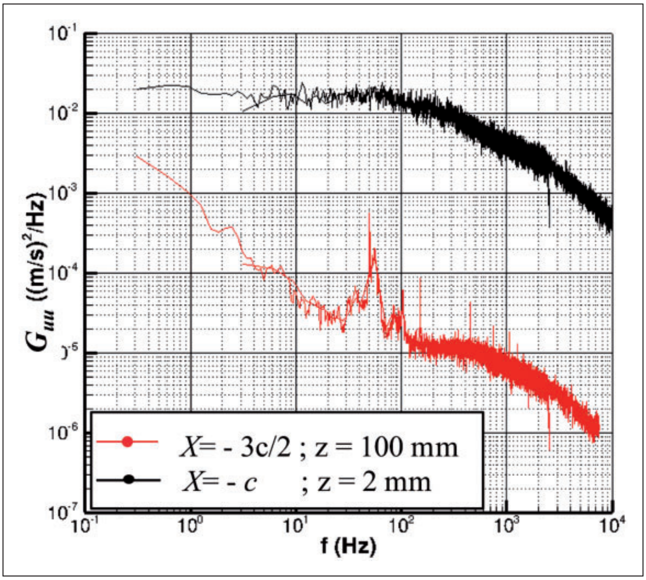

Figure 3. Spectra in the upstream boundary layer (black) and in the unperturbed incoming flow (red): each spectrum is obtained and plotted with two frequency resolutions (0.3 Hz and 3 Hz).

than 2.5%. This was not the case in Jacob et al.,[1] where the interaction source was probably responsible for a large part of the background noise resulting in a very low signal-to-noise ratio for the tip clearance noise.

Boundary layer spectra. Boundary layer spectra have been obtained both from HWA and LDV. A typical result obtained from HWA is displayed on Figure 3 with two frequency resolutions (0.3125 and 3.125 Hz) and 20 averages each. The spectra shown on this figure are obtained in the casing plate boundary layer upstream of the airfoil and in the unperturbed external flow. The latter have a very low turbulence level: therefore, some low frequency noise sources peak out from the broadband spectrum between 30 and 200 Hz typically but are not recognisable in the boundary layer spectra. Their physical origin will be discussed later.

C_p at mid-span: tuning the AoA

The pressure distribution at mid-span helps to determine the angle of attack in order to meet similar airfoil loading conditions as those reported in Jacob et al.[1] These are highly dependent

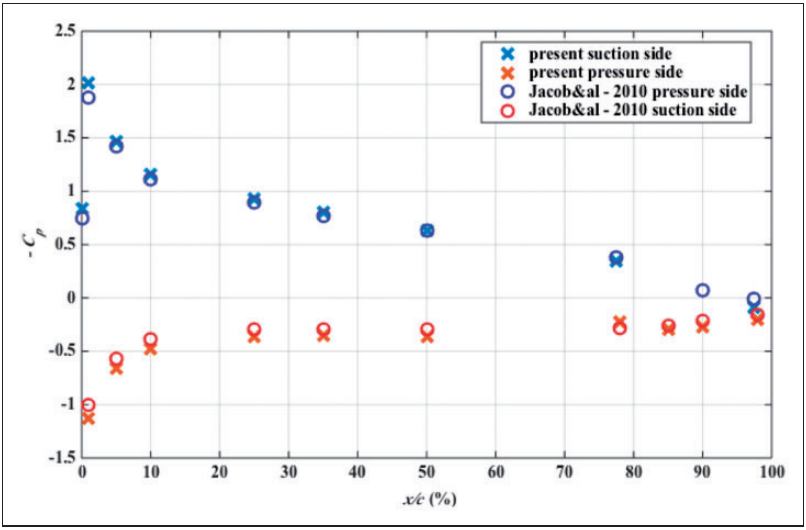

Figure 4. C_p distribution at mid-span. Comparison with the results of Jacob et al.[1]

on the upstream conditions. Since in the present case the upstream shear flow turbulence and the boundary layers have been reduced, the choice was made to adapt the airfoil angle of attack in order to keep the same C_p distribution. As a result, the angle of attack was set to $16.5 \pm 0.5°$, that is significantly higher than in the former experiment ($15° \pm 0.5°$). The C_p at mid-span shown in Figure 4 fits within 7% the C_p reported in Jacob et al.[1]

LDV measurements in the tip region

LDV measurements have been carried out in the tip region: two velocity components, the streamwise velocity u, the spanwise velocity component w, their mean values U and W as well as the rms values of their fluctuations have been measured across the TLV at various streamwise and spanwise positions along cross-stream directions from the suction side wall.

LDV set-up

The LDV measurements are carried out with a Dantec, backscatter LDV system. Two pairs of beams are used for two-dimensional velocity measurements. They are supplied by the green line (514 nm) and the blue line (488 nm) of two Coherent DPSS (Diode Pumped Solid State) 1 W Laser sources. The beams of each pair undergo a relative frequency shift of 40 MHz in a Bragg cell. The four beams are guided to the flow with an optical fibre, which is terminated by a focusing lens with a focal length of 400 mm for the gap region. The beams of each pair have a mutual angle of 5.6°. In the gap region, the size of the measurement area (i.e. the spatial resolution) is about 119 μm^2 in the measurement plane whereas its length in the cross-stream direction is about 2.4 mm. The Fringe spacing is 5.286 μm for the green line and 4.992 μm for the blue line. The backscattered beams are focused by the same lens and sent through an optical fibre onto photomultipliers. The signals are then treated by two Dantec real-time signal analysers and post-processed on a personal computer. The seeding material is vaporised paraffin injected into to wind-tunnel fan inlet, thus ensuring a homogeneous mixing throughout the flow. LDV measurements are carried

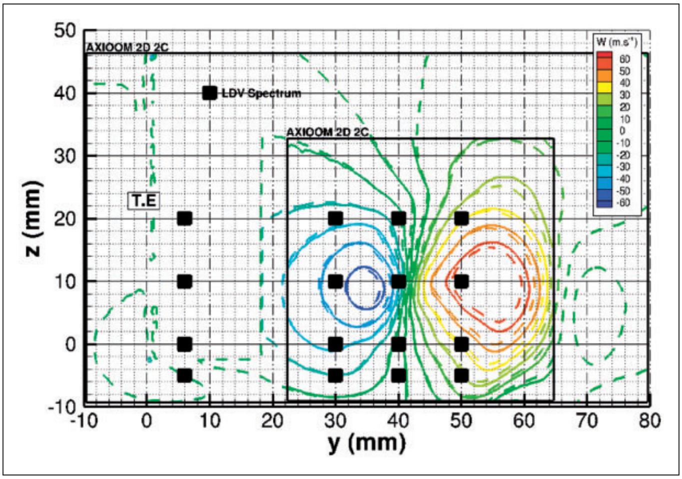

Figure 5. Velocity spectra obtained from LDV measurements in the TLV at $x = 2$ mm. (a) $y = 5$ mm; (b) $y = 30$ mm; (c) $y = 40$ mm and (d) $y = 50$ mm.

out in the same region as PIV measurements, namely around the airfoil in the gap region. They provide a useful comparison for the PIV measurements as well as spectral information.

Velocity profiles

Velocity profiles obtained from LDV are shown together with profiles extracted from PIV measurements in Figures 16 and 17, whereas errors are compared on Figure 18.

Typical spectra

Typical velocity spectra obtained from the LDV measurements in the $x = 2$ mm section are shown in Figure 6 and the location of the measurement points is plotted in Figure 5 where iso-contours of the spanwise velocity obtained from 2D-2C TR PIV are also shown in the background.

The spectra of plot (a) of Figure 6 are obtained near the airfoil trailing edge ($y = 5$ mm): they are smooth and have a relatively low level compared to those from the other plots: this suggests that TLV does not influence too much the motion near the trailing edge. Moreover, the $z = -5$mm spectrum is much lower than those obtained at $z \geq 0$: this is because it is lower than the tip clearance and therefore quiet fluid from the pressure side sweeps past this point.

Most spectra from plots (b), (c) and (d) that are obtained at the cross-stream positions $y = 30$ mm, 40 mm, and 50 mm, respectively, are dominated by a broad peak between 30 Hz and 100 Hz whose level increases as the probe approaches the vortex core. Moreover, these peaks are stronger on the airfoil facing side of the TLV (b) than on the side facing the outer flow (d). This suggests that the peak might be due to a mechanism related to the TLV rather than to the surrounding jet. The peak is also present in the inflow spectrum of Figure 3, but three orders of magnitude smaller than in the TLV: it could be the sound generated by the mechanism that appears on the inflow spectrum of the otherwise unperturbed upstream but there is no further evidence for such an interpretation.

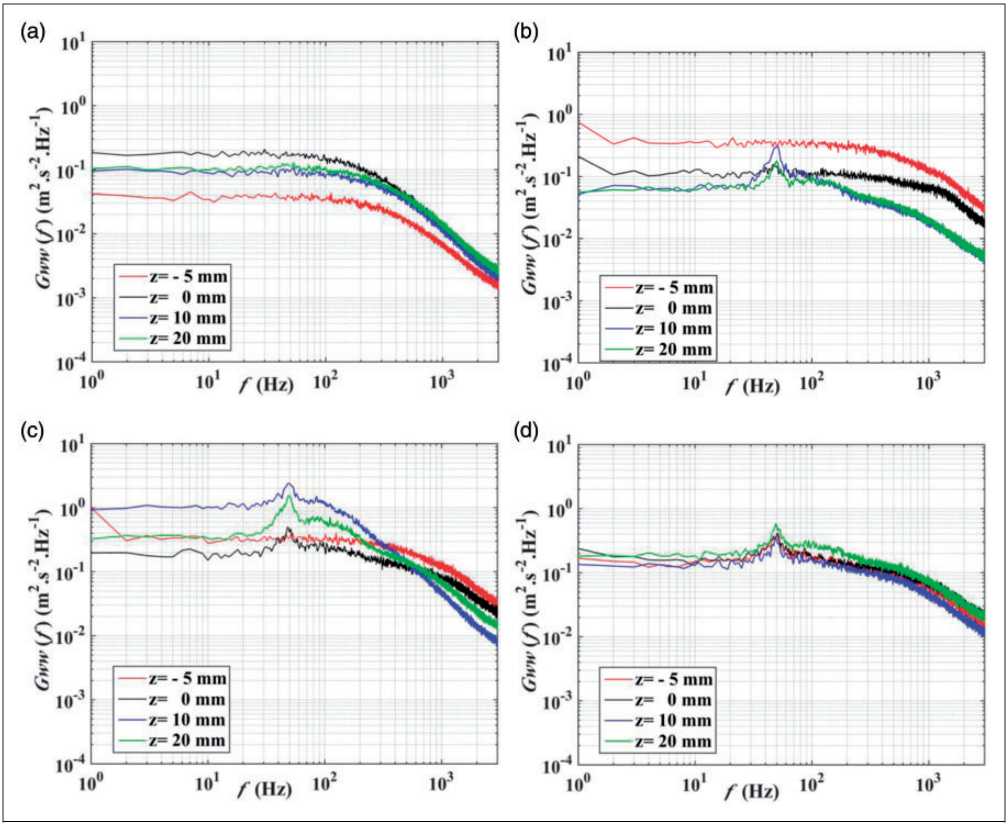

Figure 6. Locations of the measurement points corresponding to the spectra of Figure 5.

Another interesting observation of these spectra is that the points near the casing plate are less (or even not) affected by the low frequency phenomenon than the points away from the wall. The unperturbed "layer" decreases away from the airfoil. The reason for this is unclear, as no physical explanation for this peak has been found so far.

2D-2C TR-PIV measurements

First two-dimensional–two-component time resolved (2D-2C TR) PIV measurements have been carried out in the TLV region at various streamwise stations. The measurement planes are cross sections of the TLV as it rolls up from the suction side tip edge into the downstream direction, almost parallel to the x-direction (Figure 7).

2D-2C PIV set-up

For the measurement of the cross-stream velocity components v, w in a cross-stream plane (y, z), the light sheet was parallel to this plane. The Laser source was placed on the suction side pointing towards the airfoil as shown on Figure 8. In order to minimise light reflections, the airfoil was painted in black. The source was a *Quantronix* Dual Cavity Laser that could

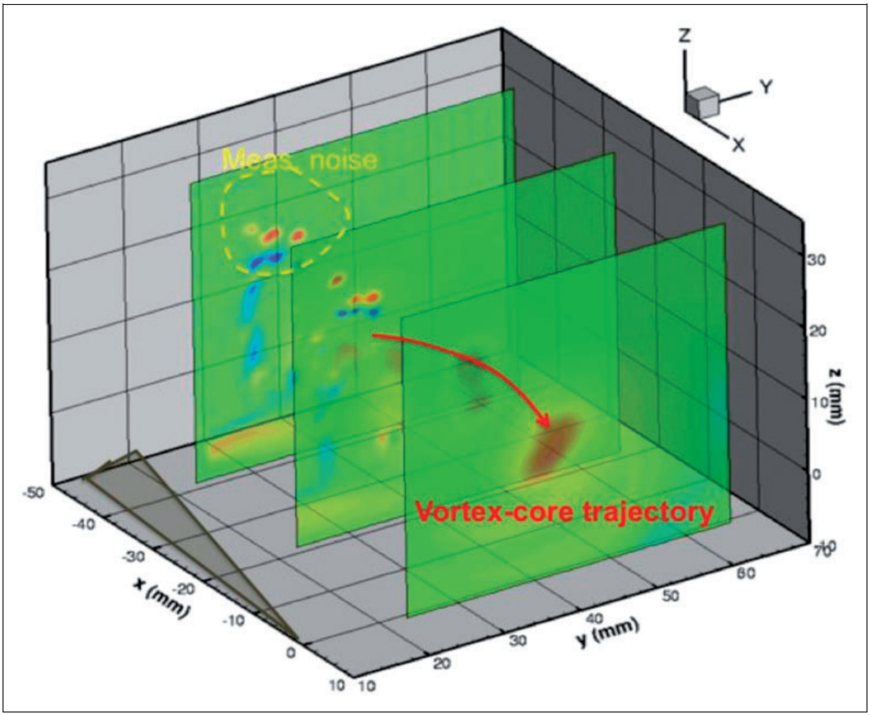

Figure 7. TVL roll-up in three cross sections obtained from 2D-2C PIV: $x = -40$; -20 and $+200A0$mm: the trace of the airfoil on the casing plate is shown on the left part of the plot in dark grey. The mean streamwise vorticity component is plotted; red corresponds to anti-clockwise and blue to clockwise rotation. The spots surrounded by a yellow circle correspond to measurement noise. It can be seen that the vortex is almost parallel to the x-direction, i.e. it roughly follows the direction of the upstream flow.

be directed *via* a mobile arm. The flow was seeded in the same manner as for the LDV measurements at the inlet of the wind-tunnel fan, ensuring a homogeneous mixing throughout the flow. The Phantom V12 fast camera was placed in the flow downstream of the test section, its axis facing the TLV. The 100 mm lens had to be cleaned every 5 s, that is, every 14,000 to 37,000 snapshots because of the paraffin condensation. The views are oriented from downstream to upstream and the sign of rotation is defined in that context. Velocity is computed on 12×12 px spots by an iterative algorithm with 50% overlap. The resulting physical velocity field resolution is about 0.4 mm in each direction.

Three cross-stream sections of the TLV in the gap region were considered: $x = -40$ mm that is, one-fifth chord upstream from the Trailing Edge (TE), $x = -20$ mm, one-tenth chord upstream from the TE, and $x = 2$ mm, the latter being slightly downstream of the TE, almost in the same cross section.

The default image window was a 608×600 px field roughly centred on the TLV core, covering a $42\,\text{mm} \times 42\text{mm}$ window of the $y - z$ plane: in a given cross section, 36,500 image-pairs were obtained from a set of five data series each made of 7300

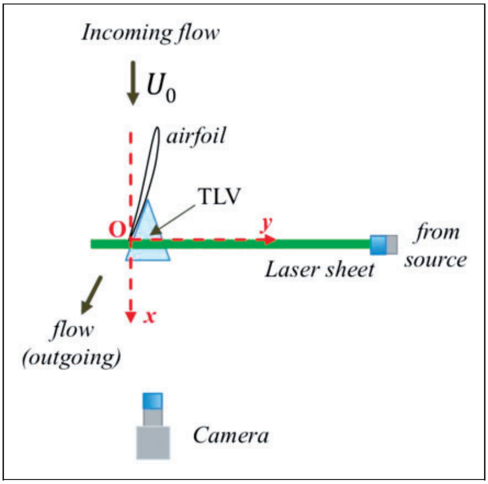

Figure 8. Set-up for 2D-2C TR-PIV measurements. The camera is oriented towards the incoming flow and the TLV axis; the lens receives airflow despite the flow deviation by the airfoil. The sketch illustrates the set-up for measurements in the $x = 2$ mm plane.

image-pairs acquired at a 7 kHz rate. For these high frequency measurements, the separation between two images was $\Delta t = 5$ μs in order to obtain a relative particle displacement above 5 px.

In the downstream section $x = 2$ mm, data were also collected in a larger domain with a 1280×800 px matrix surrounding the TLV core, covering a 90 mm × 56 mm field of the $y - z$ plane. In this $x = 2$ mm cross section, 13,900 image-pairs were obtained from a set of five data series each made of 2780 image-pairs acquired at the rate of 3 kHz. The size of this domain allowed an insight into the tip/TE edge region as well as into the pressure side region. Most results shown here are obtained in this domain.

The 2D-2C PIV set-up is illustrated on Figure 8.

Mean flow

Mean and rms velocity components. In this section, results are shown in the $x = 2$ mm section. The results for both image sizes are compared on their shared area in Figure 9. Iso-contours of the mean velocity and of its fluctuations are plotted. First it can be observed that the contour lines agree very well despite the fact that the PIV system did not have the same setting for both image sizes. This gives confidence as to the reproducibility of the 2D-2C TR PIV measurements.

As to the content, the typical features of an anti-clockwise rotating vortex can be seen in this section of the TLV. In the right part of the plots, a second weaker vortex can be guessed, corresponding to a second relative maximum of the velocity fluctuations, but it does not appear very clearly and its sign cannot be told from Figure 9. The rectangular lines in the left part of the plots define the contours of the airfoil as seen from the camera but they have no physical meaning in terms of velocity since the signal in this region is perturbed by light reflections. The trailing edge (TE) corresponds to $y = 0$.

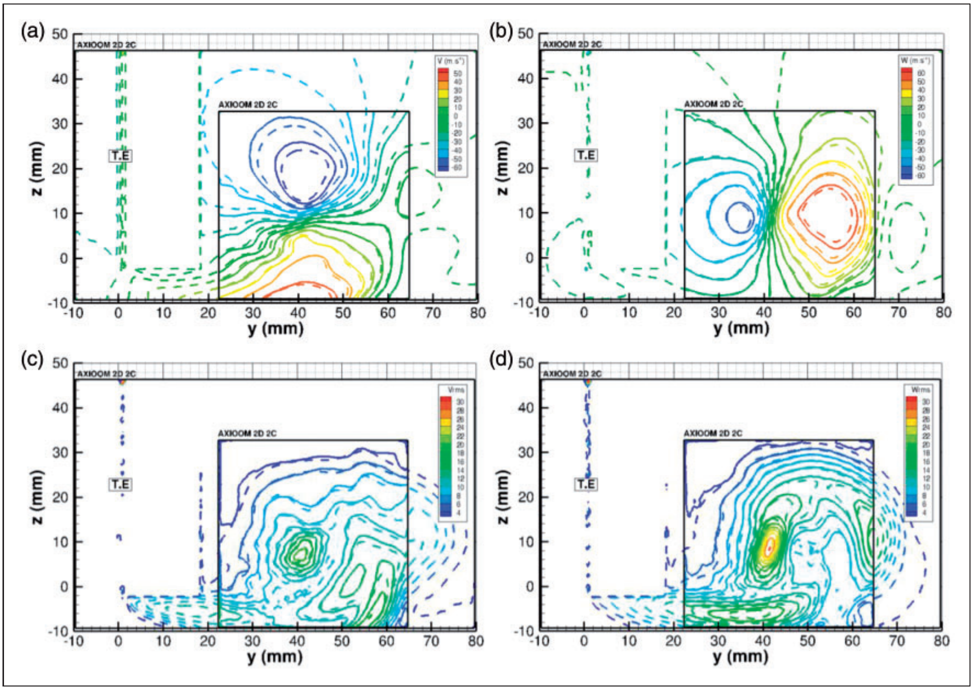

Figure 9. 2D-2C TR PIV in the $x = 2$ mm section for the two measurement windows. Iso-contours of the mean velocity components V plot (a), W (plot (b) and the rms values of their fluctuations V_{rms} and W_{rms} on plots (c) and (d), respectively. Large window: dashed lines, small window: solid lines.

Mean vorticity and NAM. The mean vorticity in the $x = 2\,\mathrm{mm}$ section is plotted on Figure 10(a). On this plot, several vortical structures can be identified: a large anti-clockwise vortex, which is the TLV; on its outward facing side (right), there is another counter-rotating vortex, which is due to fluid entrained by the TLV. Finally, anti-clockwise vorticity can be seen in the tip clearance that is due to flow separation on the pressure side of the blade. The latter is the mechanism that occurs along the whole pressure side and feeds the TLV. Note that the vorticity appearing on the blade surface (rectangular shape) cannot be interpreted as the light reflections flaw the signals in the blade vicinity. The vorticity indicates how the various vortices are located in the flow and it is possible to deduce their strength by integration. However, vorticity is neither appropriate to precisely determine the vortex centre when the cross-section is not elliptic, nor ideal to determine the boundaries of the vortex.

In order to identify the centre of a vortical structure and its spatial extent, two tools based on the concept of Normalised Angular Momentum (NAM) have been developed in the past, namely the functions Γ_1 and Γ_2.[7,8]). The two functions consider only the topology of the velocity field and smooth out the small-scale turbulent intermittency.

The vortex centre identification function Γ_1 at a fixed point P is defined as the NAM based on the absolute velocity as follows

$$\Gamma_1(P) = \frac{1}{S}\int_{M\in S} \frac{(PM \wedge U_M)\cdot \mathbf{x}}{\|PM\| \cdot \|U_M\|}\,\mathrm{d}S$$

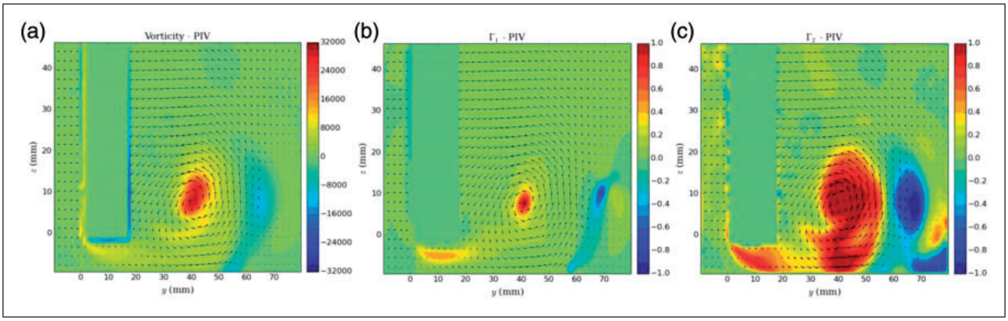

Figure 10. Mean vorticity: plot (a), Γ_1: plot (b) and Γ_2: plot (c), in the $x = 2$ mm section. Mean velocity vectors are also shown to show the local in-plane flow direction.

where S is a two-dimensional area surrounding P and $\mathbf{x}$ is the unit vector normal to the plane (here the streamwise direction). $|\Gamma_1|$ is a dimensionless scalar bounded by 1. This bound is reached at the vortex centre and the sign of Γ_1 indicates the direction of its rotation and Γ_1 appears as the absolute NAM.

Similarly, the vortex boundary identification function Γ_2 is derived from relative velocity field, by taking into account a local convection velocity $\tilde{U}_P$ around P

$$\Gamma_2(P) = \frac{1}{S} \int_{M \in S} \frac{[PM \wedge (U_M - \tilde{U}_P)] \cdot \mathbf{x}}{\|PM\| \cdot \|U_M - \tilde{U}_P\|} \, \mathrm{d}S$$

where $\tilde{U}_P = \frac{1}{S} \int_S U \, \mathrm{d}S$. Thus Γ_2 appears to be a relative NAM.

Since the velocity field of the PIV measurements is sampled at discrete spatial locations, the two functions are approximated in the post-processing by

$$\Gamma_1(P) = \frac{1}{N} \sum_S \frac{(PM \wedge U_M) \cdot z}{\|PM\| \cdot \|U_M\|}$$

$$\Gamma_2(P) = \frac{1}{N} \sum_S \frac{[PM \wedge (U_M - \tilde{U}_P)] \cdot z}{\|PM\| \cdot \|U_M - \tilde{U}_P\|}$$

where N is the number of points M inside S.

These two functions are applied to the 2D-2C TR PIV field obtained in the $x = 2$ mm plane and plotted in Figure 10(b) and (c). Velocity vectors are also indicated on these plots. The rectangles without vectors correspond to the airfoil as seen by the fast camera. Compared to plot (a), the function Γ_1 gives a much narrower spot around the vortex centre position. In fact the vortex centre can be determined much more precisely since it corresponds to maximum of Γ_1. In the present case, the two vortex centres are found at $(y, z) \approx$ (41 mm; 7.8mm) and at $(y, z) \approx$ (69 mm; 10mm). The vortex boundary identification function Γ_2 shows that the two vortices are much larger than the region of high vorticity. The TLV is connected to the flow past the tip clearance. It is noteworthy that the secondary vortex "guessed" on the velocity plots is clearly identified with these identification tools. This vortex is due to entrainment of fluid from the boundary layer by the TLV rotation.

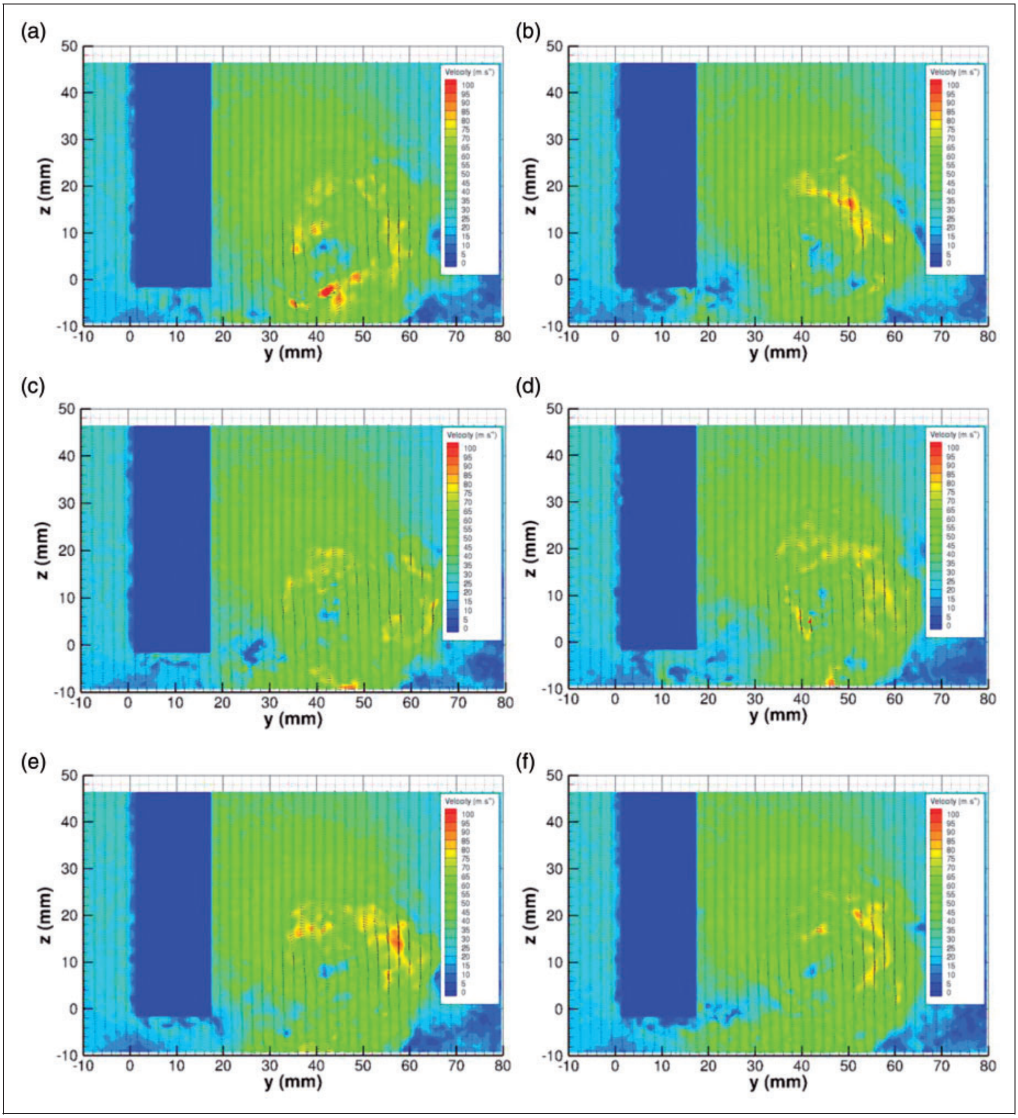

Figure 11. Snapshots of the instantaneous velocity (modulus and vectors) in the large domain obtained at a 3 kHz rate. (a) t_0; (b) $t_0 + 0.33$ ms; (c) $t_0 + 0.66$ ms; (d) $t_0 + 1.00$ ms; (e) $t_0 + 1.33$ ms and (f) $t_0 + 1.67$ ms.

Unsteady flow

In order to give an idea about the instantaneous flow that provides the statistics discussed so far, a few snapshots of the flow field are shown in this paragraph. The snapshots are gathered on plots (a) to (f) of Figure 11 and display six consecutive maps of the instantaneous 2D velocity modulus associated with the local instantaneous velocity vectors. In order to provide an insight into the flow near the gap (the measurement plane is slightly downstream of the airfoil), results are shown for the large domain, thus the sampling frequency is 3 kHz and the snapshots are generated every 0.33 ms.

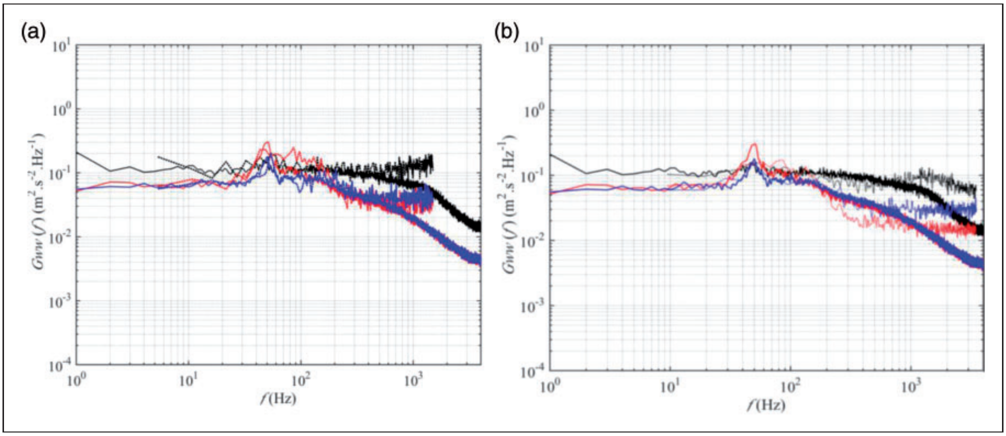

Figure 12. Comparison of PIV a LDV spectra at x = 2 mm and y_0 = 30 mm. Line: LDV; dotted line: PIV. z = 0 (black), z = 10 mm (red); z = 20 mm (blue). (a) Comparison with 3 kHz PIV (b) Comparison with 7 kHz PIV.

On these plots it is interesting to underline the strong variability of the flow at successive instants. The vortex rotation can be guessed when comparing successive snapshots, although it must be kept in mind that the structures shown on the plots also move at high speed in the normal-to-plane (x) direction. The maximal velocity exceeds sporadically 100 m/s but at isolated spots, where the average is rather around 50 m/s (see Figure 9). At such points, the velocity may drop down to very low values ($< 40 - 50$ m/s) a few moments later. Another interesting point is the blue spot oscillating around (42 mm; 10 mm) that corresponds to the TLV centre. The oscillatory motion of the TLV centre is a feature to investigate in more detail that is beyond the scope of the present paper.

Spectra obtained by PIV confirm the trends shown by the LDV analysis. In Figure 12, PIV spectra G_{ww} of the vertical velocity fluctuations w obtained at $x = 2$ mm and $y = 30$ mm with two sampling frequencies (3 kHz and 7 kHz) are compared with LDV spectra shown on Figure 6(b) at three of the vertical positions displayed in Figure 5.

In the low frequency range (up to $\sim$ 0.5 kHz), the PIV and LDV spectra are quite close. The low frequency peak is more or less pronounced on the PIV spectra, depending on the vertical position: at the highest point, $z = 20$ mm, i.e. 20 mm above the trailing edge corner, the peak is well captured by the PIV measurements. The decrease at higher frequencies, however, is not well captured by the PIV measurements. This is partly due to aliasing as can be seen when comparing the plots (a) and (b) of Figure 12 that are obtained for different sampling frequencies. Therefore, the discrepancy may partly be mended by using an anti-aliasing filter. This also seems to indicate that aliasing starts well below de Nyquist frequency, which shows that the rapid flow changes are difficult to approach quantitatively using PIV. This holds especially in the present situation where the normal-to-plane flow reaches high speeds and the smoke particles cross the PIV plane in a very short time.

2D-3C TR PIV set-up

Time-resolved PIV measurements were also carried out for the three velocity components in 2D regions (stereo – TR PIV). For the purpose of comparison, the measurement planes were

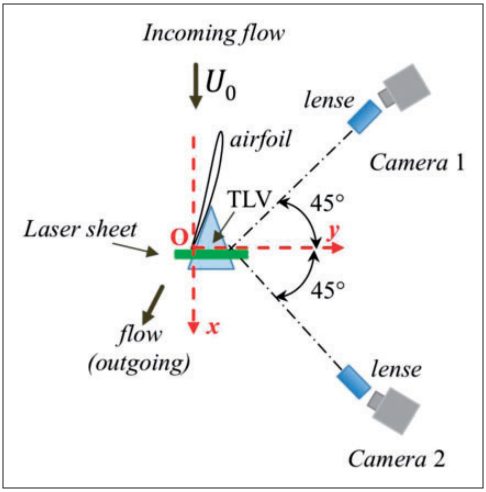

Figure 13. Set-up for 2D-3C TR-PIV measurements. The source is located beneath the casing plate that is equipped with a glass window. The cameras are oriented with a 45° angle towards the measurement plane. The sketch illustrates the set-up for measurements in the $x = 2$ mm plane.

the same as for the 2D-2C TR PIV. Moreover, since 2D-3C is very difficult to tune properly, it could thus be validated against the 2D-2C TR PIV results.

For the measurement of three velocity components u, v, w in a cross-stream plane (y, z), the Laser source was associated with two high speed cameras in order to obtain the off-plane velocity component U across the light sheet. In order to minimise light reflections on the airfoil, the Laser source was placed under the casing plate that was equipped with a glass window. The source was a *Quantronix* Dual Cavity Laser that could be directed *via* a mobile arm. Here also the flow was seeded with vaporised paraffin at the inlet of the wind-tunnel fan. The two Phantom V12 fast cameras were equipped with 135 mm lenses. They were placed on the suction side downstream and upstream of the airfoil pointing towards the TLV region as shown in Figure 13. The lenses made a 45°angle with respect to the test section on each side of it. Thus the sheet only marginally impacted the part of the airfoil facing the cameras. Each camera was equipped with a Scheimpflug support to compensate for angular distortion. Velocity was computed on 12 × 12 px spots by an iterative algorithm with 50% overlap.

The default image window was a 608 × 600 px field centred approximately on the TLV core, covering a 50 mm × 25mm field of the $y - z$ plane: in a given cross section, $2 \times 36,500$ image-pairs were obtained from a set of five data series each made of 7200 double image-pairs acquired at a 7 kHz rate.

However, in the downstream section $x = 2$ mm, a few measurements were also carried out on a larger domain (800 × 800 px) for each camera surrounding the default domain at a $3 - 4$ kHz rate in five sets of 3900 double image pairs. The resulting physical domain covers a 69 mm × 38 mm region.

The 2D-3C PIV set-up is illustrated in Figure 13.

Mean and rms velocity

The 2D-3C mean velocity field is plotted in Figures 14 and 15.

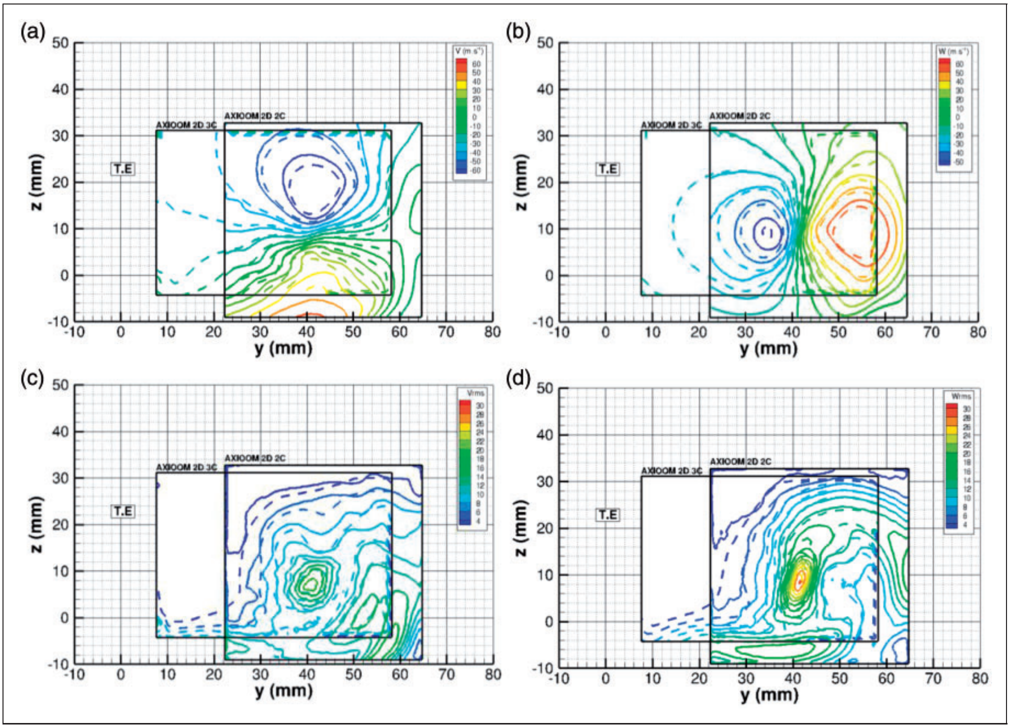

Figure 14. Comparison of 2D-2C and 2D-3C PIV on the cross-stream components. Plot (a): iso-contours of V; plot (b): iso-contours of W; plot (c): iso-contours of V_{rms}; plot (d): iso-contours of W_{rms}

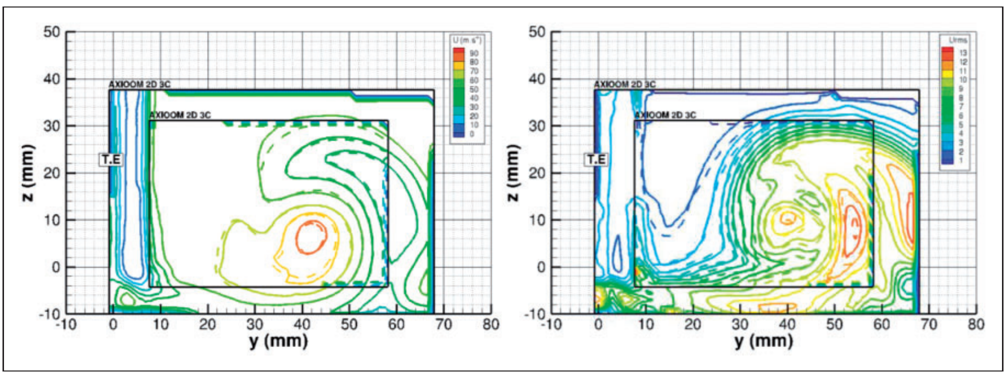

Figure 15. Comparison of the 2D-3C PIV streamwise components for the large (solid lines) and the small (dashed lines) window. Left plot: Iso-contours of U; right plot: Iso-contours of U_{rms}.

In Figure 14, the iso-contours of the mean velocity and its fluctuations are plotted for the cross-stream components v and w. Both PIV approaches are compared. They agree remarkably well: this is a strong confidence indicator for the stereo-PIV (3C) approach, as the set-up is much more complicated and difficult to tune than for classical two component PIV: indeed, the adjustment of the two cameras and their focus on the same region of space are major challenges. Here the iso-contours of mean and rms values of v and w almost superimpose over the whole shared domain.

For the streamwise component of the 2D-3C TR PIV, the other PIV technique does not provide comparison data. Therefore, a comparison of the streamwise velocity obtained from the large and the small domain is plotted in Figure 15. Again the iso-contours fit almost perfectly despite the fact that the cameras had to be recalibrated and the acquisition parameters adapted, when changing from one domain to the other. It is interesting to observe that the streamwise velocity diminishes considerably but remains positive near the airfoil although it is not really a surprise: the test section is slightly downstream of the TE and therefore one would not expect any flow reversal.

The other interesting point about the mean streamwise velocity is that it becomes very large near the vortex centre where it reaches about 90 m/s (30% above U_0). The streamwise fluctuations have several maxima: there is a region between 35 and 58 mm, where the fluctuation level is quite high, with local maxima. This region weakens and extends further to the

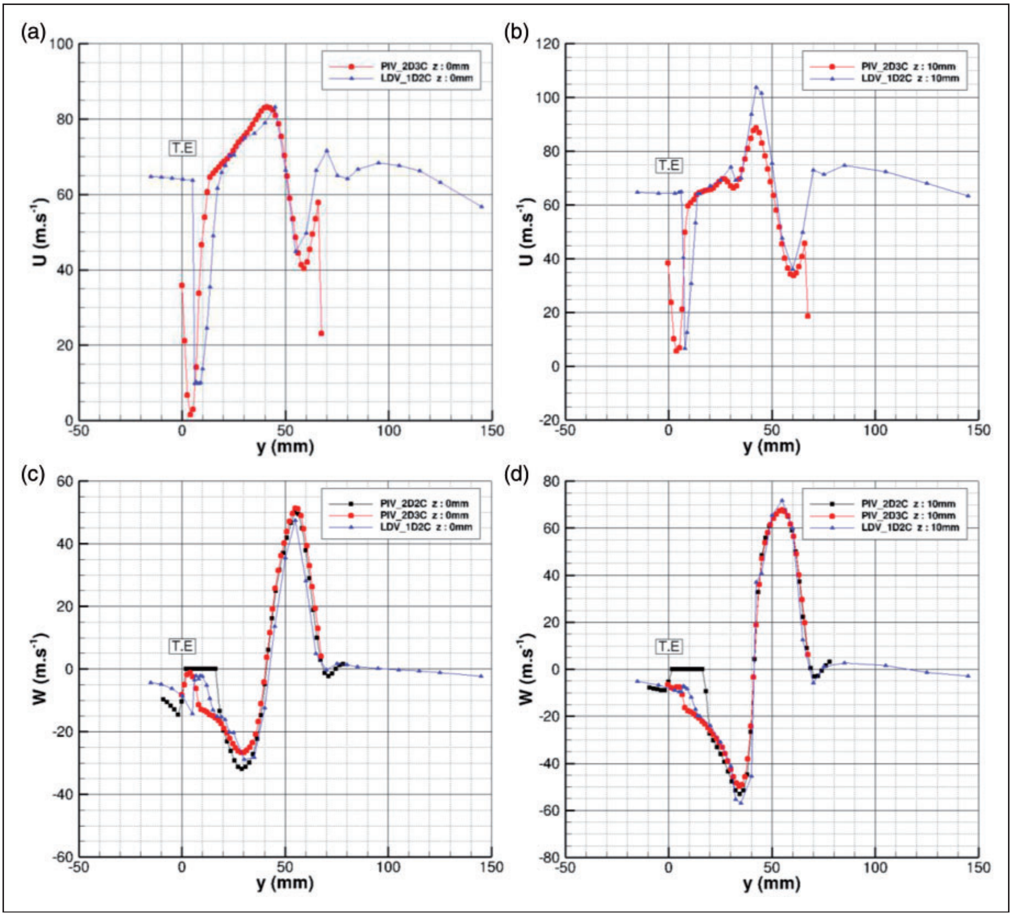

Figure 16. Comparison of streamwise and spanwise mean velocity profiles in the cross-stream direction, obtained by PIV and the LDV

airfoil at $z = -h/2$, just as in Figure 6.c of Jacob et al.[1] Another region of high streamwise fluctuations at $z \sim h$ starts about $y > 65$ mm. This region is incomplete because the right limit of the large PIV domain is reached: the only fact that can be observed is that this region does not appear at $z = -h/2$ for $y < 65$ mm. In Jacob et al.[1] Figure 6(c), obtained at $z = -h/2$, this region appears indeed to be further out in the flow.

Comparing PIV with LDV

PIV and LDV results are compared for two streamwise and spanwise velocity profiles in the cross-stream direction on Figures 16 and 17.

The mean velocity at two spanwise positions of the $x = 2$ mm plane and the rms value of the corresponding fluctuations, respectively, are displayed. For the streamwise velocity component, only 2D-3C PIV can be compared to LDV, whereas for the spanwise component, the 2 PIV approaches and the LDV can be compared.

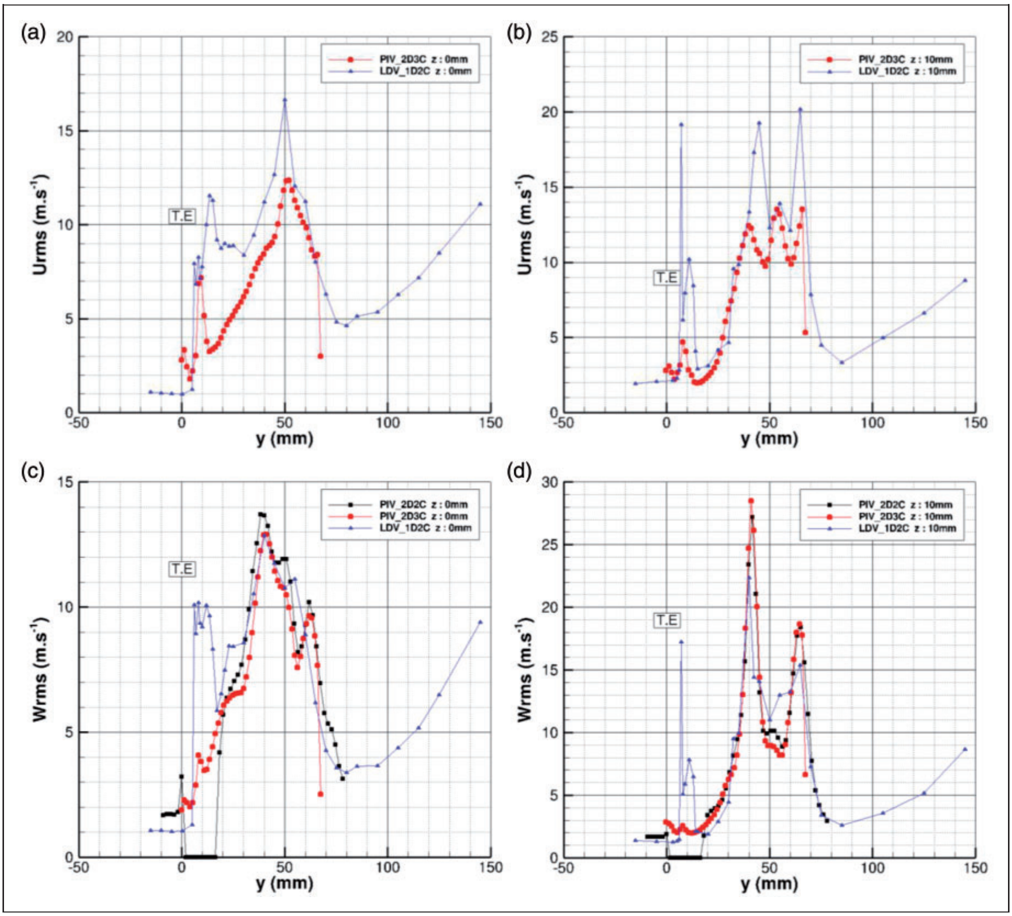

Figure 17. Comparison of streamwise and spanwise velocity fluctuation profiles in the cross-stream direction, obtained by PIV and the LDV.

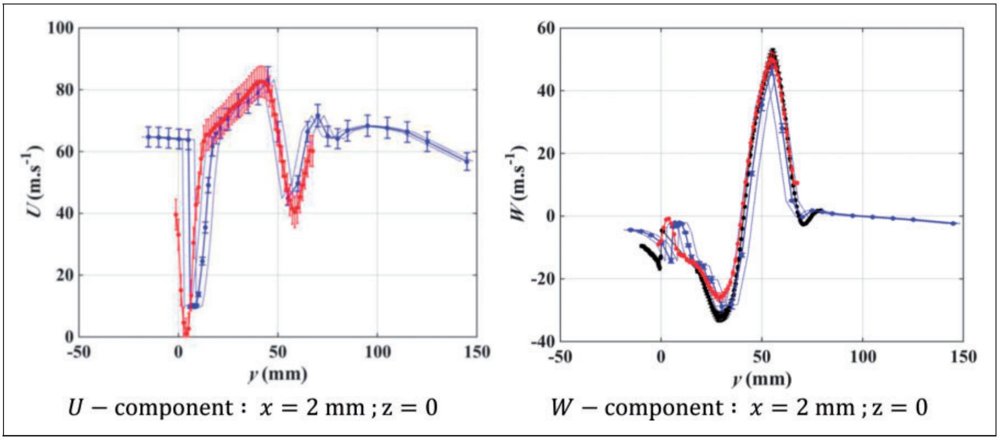

Figure 18. Error estimates on the mean streamwise and spanwise velocity components U and W, for the LDV (blue), 2C PIV (black) and 3C PIV (red) measurements. The dotted lines indicate the error bounds on the y position: they have been summed up for the LDV component for the sake of clarity. The region where no spanwise velocity was found in the 2C PIV has been removed since it is due to reflexions.

The agreement between PIV and LDV data is excellent for the spanwise velocity and its fluctuations except in the vicinity of the airfoil, where light reflections perturb some of the data. This is obviously the case for the 2D-2C PIV measurements. There is also uncertainty about the velocity fluctuations in this region: the airfoil near wake turbulence is obviously underestimated by both PIV approaches.

Similar conclusions can be drawn about the streamwise velocity: the two estimates of U collapse very well, except for the $\Delta y \sim \pm 3$ mm offset between the peak values of the PIV and the LDV: a possible explanation would be that the two measurements were not carried out exactly in the same plane, and since the wake is oblique, turned to the decreasing y, its deepest point moves accordingly. The TLV grows as it moves downstream: therefore its maximum U moves to smaller values of y, whereas its minimum moves towards increasing values of y. This is exactly the trend that can be seen between the blue and the red profiles (Figure 16(a) and (b)). Consequently, the PIV plane would be somewhat further downstream than the LDV axis. Only the amplitudes (wake depth, vortex max/min) do not fit into that scheme, since they should all (slightly) decrease, whereas they do not follow a clear trend. Another factor explaining y-offset is that the length of the LDV control volume in the y-direction is about 2.4 mm. The last factor is that the PIV probes and light sheets are positioned without flow: when the flow is started, the whole test section is slightly shifted to the suction side because of the strong lift, whereas the Laser probe is on a fixed support. This is not the case with the LDV measurements for which the tuning is carried out in the presence of the flow. The peak values of U_{rms} predicted by LDV are about 50% higher and the results are hardly compared in the wake. The reason is unclear but one should keep in mind that the streamwise velocity in the stereo PIV approach is measured for particles crossing the light sheet thickness: this is an intrinsic source of error since the crossing time is necessarily very short.

Error estimates both in amplitude ($\sim$5%) and in the y coordinate ($\pm$3 mm) are plotted in Figure 18 for the two mean flow components at the $z = 0$ position (corresponding to

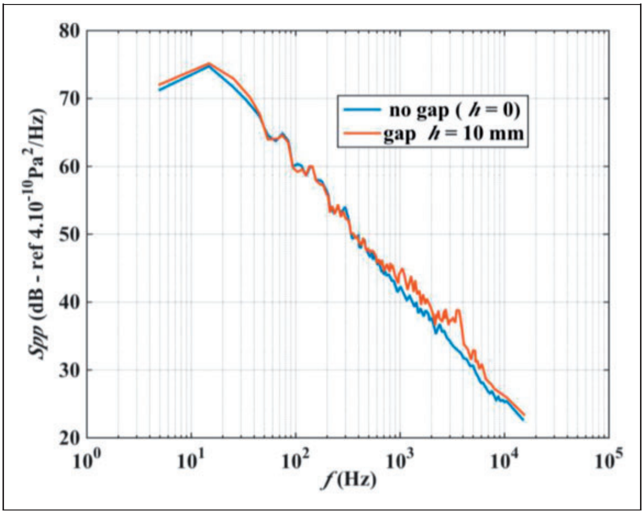

Figure 19. Far field at 2 m and 90° from the airfoil suction side. Blue: without gap. Red: with $h = 10$ mm gap.

Figure 16(a) and (c)). Figure 18 shows that the 2C and 3C PIV planes as well as their coordinates are well defined with respect to each other. The remaining differences between the three approaches are likely to be due to the error on the streamwise position that cannot be estimated properly since measurements have not been carried out in neighbouring planes.

As far as levels are concerned, the high values lie within the error bar, whereas the lowest values are not equally represented by the three approaches. Nevertheless, the comparison between PIV and LDV gives very good overall results and one has to be aware of the stereo-PIV limits.

Far field measurements

The acoustic far field was measured with a Bruel & Kjäer ½″ Microphone that was placed 2 m away from the suction side, forming a 90° angle with the mean flow direction. The measurement was repeated after removing the gap in order to compare the noise with *vs.* the noise without gap.

The resulting power spectral density is plotted in Figure 19: the gap induces a non-negligible sound emission between 0.7 and 7 kHz approximately. The noise with gap peaks out as much as $\sim$6 dB near 3.5 kHz. This measurement confirms the observations made in Jacob et al.,[1] but with the improved test rig the gap noise is clearly above the background noise. However, regarding the perturbation detected in the range $30 - 100$ Hz, which was interpreted as an oscillation of the TLV, no evidence of it is found in the far field spectrum.

Conclusions

The experiment described in this paper is a continuation of the experiment presented in Jacob et al.[1] but for minor changes. It corresponds to a novel type of configuration that has not been studied elsewhere. Moreover, the TR-PIV measurements, and more specifically the 2D-3C TR PIV (or stereo-TR PIV) discussed here are quite new techniques that have not often been applied to such a complex configuration at such high speeds. Although the benefits of the time resolution have not yet been much exploited, the feasibility of such measurements as well as the quality of the data have been assessed by cross-checking the results obtained from various techniques.

One outcome of these measurements is that results found in the earlier experiment are confirmed. In particular, earlier investigations indirectly characterised the TLV since the velocity components v and w were not measured as they were this time: thus only a footprint of the TLV was evidenced.[1] This has now been improved by carrying out PIV measurements in the plane normal to the main flow direction, which was challenge that required a dedicated experiment.

The other major achievement was to increase the signal-to-noise ratio of the tip noise, which was achieved by reducing the boundary layer thickness as well as its interaction with the leading edge and by reducing the main flow noise at the edges of the supporting plates, using brushes.

Among the findings of this experimental campaign, there is a low frequency oscillation of the TLV, whose mechanism is yet unclear but which does not seem to significantly radiate into the far field. Additionally, a clear hump at medium and high frequencies ($0.7 - 7$ kHz) is found in the far field, that confirms the conclusions of Jacob et al.[1] and that is also found in the paper of Boudet et al.[5]

Moreover, the data set generated in this experiment is suitable for comparison with unsteady CFD such as LES. This is the point of the paper by Boudet et al.,[5] which could be seen as part two of the present paper since it examines and validates a LES against the data presented herein.

Finally, the results for this non-rotating geometry might be partially extended to rotating blades as far as the self noise generation mechanisms of a blade are considered: the interaction of the unsteady tip vortex with the edges of the blade. For rotating blades, two additional mechanisms might be encountered, which are not covered by the present study: interactions of the TLV with neighbouring blades and possible rotating instabilities or their onset, as reported by Boudet et al.[9] and Cahuzac[10].

Declaration of conflicting interests

The author(s) declared no potential conflicts of interest with respect to the research, authorship, and/or publication of this article.

Funding

This work has been carried out in the frame of the Sino-French project AXIOOM, funded by ANR and NSFC. It was also conducted in the framework of the LabEx CeLyA ("Centre Lyonnais d'Acoustique") of the Université de Lyon, operated by the French National Research Agency (ANR-10-LABX-0060/ANR-11-IDEX-0007).

References

1. Jacob MC, Grilliat J, Camussi R, et al. Aeroacoustic investigation of a single airfoil tip leakage flow. *Int J Aeroacoust* 2010; 9: 253–272.
2. Bilka MJ, Anthoine J and Schram C. Measurement and analysis of radiated sound from a low speed fan with a large tip gap. *J Acoust Soc Am* 2014; 135: 2591–2595.

3. Galindo J, Tiseira A, Navaro R, et al. Development and validation of a radial variable geometry turbine model for transient pulsating flow applications. *Energy Convers Manage* 2014; 85: 190–203.
4. Pardowitz B, Tapken U, Neuhaus L, et al. Experiments on an axial fan stage: time-resolved analysis of rotating instability modes. *J Eng Gas Turbine Power* 2015; 137(6): 062505-062505-9. DOI: 10.1115/1.4028686.
5. Boudet J, Caro J, Li B, et al. Zonal large-eddy simulation of a tip-leakage flow. *Int J Aeroacoust* 2016. DOI: 10.1177/1475472X16659215.
6. Camussi R, Grilliat J, Caputi-Gennaro G, et al. Experimental study of a tip leakage flow: wavelet analysis of pressure fluctuations. *J Fluid Mech* 2010; 660: 87–113.
7. Michard M, Graftieaux L, Lollini L, et al. Identification of vortical structures by a non-local criterion: application to PIV measurements and DNS-LES results of turbulent rotating flows. In: *11th Symposium on turbulent shear flows*, Grenoble, France, 8–10 September 1997.
8. Graftieaux L, Michard M and Grosjean N. Combining PIV, POD, and vortex identification algorithms for study of unsteady turbulent swirling flows. *Meas Sci Technol* 2001; 11: 1422–1429.
9. Boudet J, Cahuzac A, Kausche P, et al. Zonal large-eddy simulation of a fan tip-clearance flow with evidence of vortex wandering. *J Turbomach* 2015; 137(6): 061001-061001-9. DOI: 10.1115/1.4028327.
10. Cahuzac A. Aspects cinétiques et acoustiques en simulation des grandes échelles et application à l′étude du contrôle de l′écoulement de jeu de jeu en turbomachines. *Thèse n° 2012-17,* 2012.

Appendix

Notation

c	airfoil chord
c_0	speed of sound in medium at rest
C_p	pressure coefficient $= -(p - p_0)\,/\,\frac{1}{2}\rho V_0^2$
e	airfoil thickness
f	frequency
G_{ww}, G_{uu}	spectral density of spanwise (w) and streamwise (u) velocity fluctuations
h	gap
H	shape factor
ℓ	airfoil span
O	origin of coordinate system located on the trailing edge/tip corner
O'	origin of coordinate system located on the casing plate beneath the leading edge
p, p_0	pressure, ambient pressure
Re_c	chord-based Reynolds number
Re_h	gap-based Reynolds number
u, v, w	instantaneous velocity components in x, y, z directions respectively
$u_{rms}, v_{rms}, w_{rms}$	root mean square of velocity fluctuations in x, y, z directions respectively
U, V, W	mean velocity components in x, y, z directions respectively
U_0	mean incoming velocity in streamwise (x) direction

x, y, z	streamwise, cross-stream (pointing away from airfoil suction side into the flow) and spanwise (from bottom (casing) plate to top) coordinates from origin O
X, Y, Z	parallel to x, y, z, but attached to origin $O\prime$
Γ_1	vortex centre identification function
Γ_2	vortex extent identification function
$\delta,\ \delta^*$	boundary layer thickness and displacement thickness
θ	observer angle (with respect to the main incoming flow direction x)
Θ	momentum thickness
ρ	air density